PINNs Augmented X-Ray Particle Velocimetry

A.M. Ali[1] and **S.A. Mäkiharju**[1]

[1]Department of Mechanical Engineering, University of California, Berkeley, CA 94720, USA

Abstract. Quantifying fluid flow non-intrusively in opaque media is achievable with x-ray particle velocimetry (XPV). However, XPV data tends to be significantly more sparse and have lower signal-to-noise ratio (SNR) than that obtained from traditional visible light particle velocimetry. Therefore, achieving the resolution needed for most flows of importance is costly or impossible with prior XPV approaches. Enhancing optical particle velocimetry data by employing Physics Informed Neural Networks (PINNs) has been shown to work well with sparse, noisy data. We present PINNs augmented XPV for simulated sparse XPV experimental data for a constant velocity flow, a constant acceleration (linear velocity) flow and a Poiseuille pipe flow. The PINN allows enhancement of XPV spatial and temporal resolutions beyond the experimental resolution. From a set of sparse, low SNR x-ray projections with low-density seeding, we can generate the experimental XPV dataset used for training and validating the PINN on a flow domain characterized by higher temporal and spatial resolution than the acquired dataset. The governing equations and boundary conditions are incorporated into the PINN's training cost function using TensorFlow that estimates the partial derivatives using automatic differentiation. The weights of the cost function are the knobs used to control the influence of experimental data, data from physics and boundary conditions on the training of the PINN.

Keywords: PINNs, XPV, multiphase flow

1. Introduction

X-ray Particle Velocimetry (XPV) can be a valuable flow measurement technique for applications where the use of conventional visible wavelength optical methods is limited due to opacity. Indeed, many multiphase flows of importance are either optically opaque due to multiple refractive interfaces (e.g., bubbly flows) or include optically opaque fluids or must utilize optically opaque containers (e.g., high power density electronics cooling systems). Initial efforts in this area have focused on adapting existing optical particle velocimetry (OPV) methods to XPV. This has proven challenging due to the low signal to noise ratio and data sparsity involved in X-ray imaging compared to OPV.

The development of X-ray particle velocimetry has been driven by advances in X-ray sources, detectors, and computational algorithms for image processing and particle tracking. As a means of overcoming the low SNR and high noise level challenges, bright synchrotrons were initially used [1]. Contrast and, hence, SNR were also improved using enhanced flow tracers [2, 3] and combined with cutting edge bright laboratory sources have achieved imaging rates on the O(1kHz) [4]. Using dimmer standard laboratory sources for XPV can be sufficient for flows which can be time resolved at O(1 Hz) scan rates. As an example, isochoric vitrifying flows can be time resolved at sub 1 Hz and since containers that are invariably optically opaque are required, due to the large temperature and pressure gradients that develop during the vitrification process, these flows can be studied using laboratory source implemented XPV [5,6].

The introduction of training a neural network using physics from governing equations as opposed to training it solely from data [7] has paved the way for extending the capabilities of OPV beyond sparse, noisy velocity data to higher spatial resolution velocity and pressure field visualizations of a 2D Taylor decaying vortex, turbulent boundary layer, compressible aerodynamic flows and biomedical flows [8, 9, 10, 11]. This approach of combining the use of PINNs with experimental particle velocimetry data

has assisted in overcoming some of the challenges of physics-informed learning such as high computational cost and limited accuracy.

2. Methods

The PINN's framework we employ is based on [7] who demonstrate the use of PINNs for learning the solution to the Navier-Stokes PDEs. The architecture consists of two main neural networks; one that is uninformed of the physics and the second that is physics informed. The first network attempts to learn the time-varying velocity and pressure field at every point in the flow domain defined at the set spatial and temporal resolution, i.e., the Navier-Stokes equations, and initial and boundary conditions while the second network solves the partial derivatives using automatic differentiation. The first network's architecture is designed to have an input layer of 4 neurons defining the flow spatial and temporal domain (x, y, z and t) followed by 15 hidden layers of 240 (4*60) neurons each and lastly an output layer of 4 neurons (u, v, w and p). The hidden layer activation function is set to sigmoid which introduces the required non-linearity to solve for the velocity field. The chosen temporal resolution for the PINN is 20x that of experimental data and the spatial resolution is 1/1000 pipe diameters. Table 1 summarizes the neural network settings.

Table 1: Neural Network Training Settings

Learning Rate	Batch Size	Training Time
10^{-4}	64	1, 2 and 4 hours (NVIDIA RTX A4500)

The cost function being optimized for the training of the networks computes the error incurred on the physics, i.e., equations labelled e in Figure 1. We modify the architecture to incorporate our simulated sparse XPV data for the flow scenarios mentioned in Section 4 instead of training using the concentration transport equation and update the cost function being optimized for the training to include the error incurred on the velocities when compared to the simulated experimental data. In addition to the error on the equations, the simulated experimental data, we also include the initial conditions and no slip boundary condition referred to as U_{BC}. As evident from the architecture deployed, we do not provide any pressure training data nor do we impose any boundary conditions on the pressure gradient. Despite that we still manage to converge to the right solution of velocities given we train our network for a sufficient amount of time.

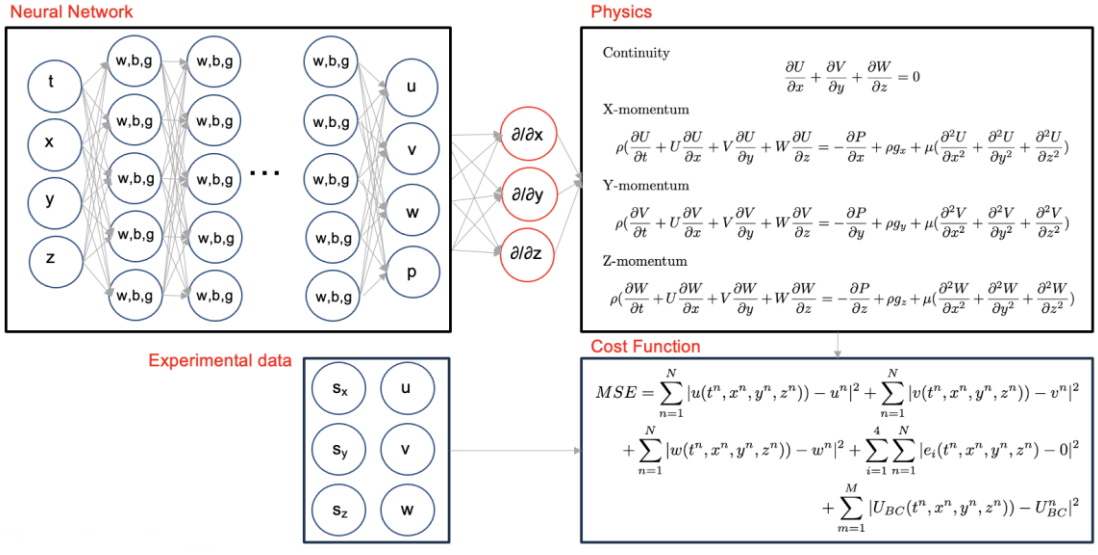

Figure 1: PINN Architecture including simulated experimental XPV data, the learning of physics from the Navier-Stokes equations and the boundary conditions

3. Experimental and Simulated Setup

Although the focus of this paper is to demonstrate the use of PINNs for extending the capability of XPV and solving for gaps in sparse and low SNR experimental data, we describe here the experimental procedure for completeness. From a single source-detector pair, we collect projections at known angles from a seeded flow with tracer particles. Figure 2 illustrates a visualization of the data collection process. As evident from the illustration, particle overlap between projections is one of the challenges with experimental data.

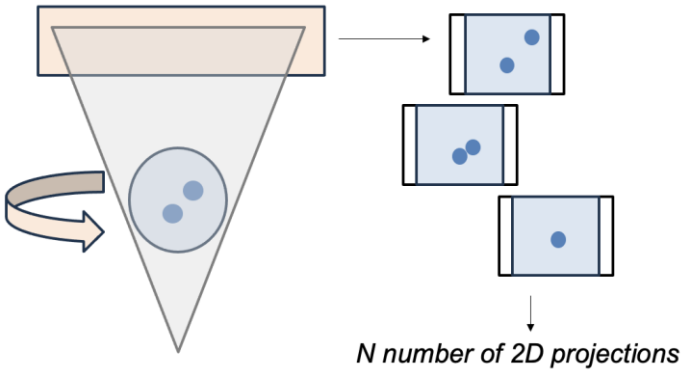

Figure 2: Experimental and simulated setup for particle velocimetry data collection where object rotates

From the acquired projections, the particles are identified using a pre-trained Region-based convolutional neural network (rCNN) on particle features. Once the particle coordinates are identified, we perform particle tracking to resolve the trajectories using a limited angle tracking approach. The resolved, sparse, branching and noisy particle tracks provide the input for our PINN. trained on synthetic data.

4. Results

4.1 Constant velocity

The simplest, trivial case we tested our code on was that with uniform velocity in order to confirm that our code was behaving as expected. Figure 3 shows the velocity profile output from the PINN. As noted the dimensionless velocities are centered around 1 which shows that the output of the PINN is equivalent to the simulated constant velocity components U, V and W respectively.

4.2 Constant acceleration

The second test case was constant acceleration, i.e. a linear velocity. The simulated U, V and W profile was now simulated to linearly increase. The output of the PINN normalized by the maximum velocity values U*, V* and W* is also shown in Figure 3. We note that the PINN here is also behaving as expected. These first two simplest of test cases provided simple sanity checks to verify our PINN architecture and do not include the use of initial and boundary conditions.

4.3 Poiseuille flow

The third case simulated for is that of a Poiseuille pipe flow. The simulation for this flow utilizes the architecture shown in Figure 1 and includes initial and boundary conditions. The flow is simulated in the laminar regime with Re = 150 and assumed to be fully developed. The maximum velocity along the centerline is simulated to be 50 mm/s and the diameter of the pipe is simulated to be 6.25 mm. Figure 4 shows the PINN's accuracy in learning the velocity profile when 100 experimental data points from 5 projections are used in the training and the PINN is trained for 4 hours. Figure 5 shows the PINNs output plotted at a single instant in time over the radius of the pipe. Training for 1 hour for Figure 5 results was sufficient.

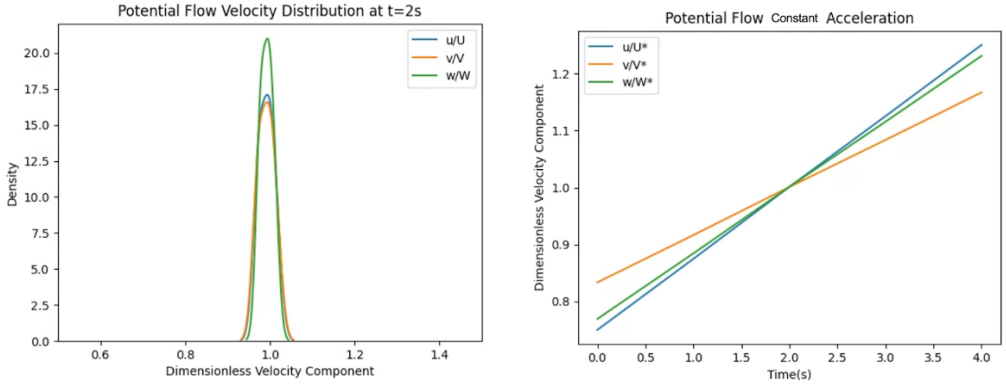

Figure 3: PINN output for constant and linear velocity flow fields

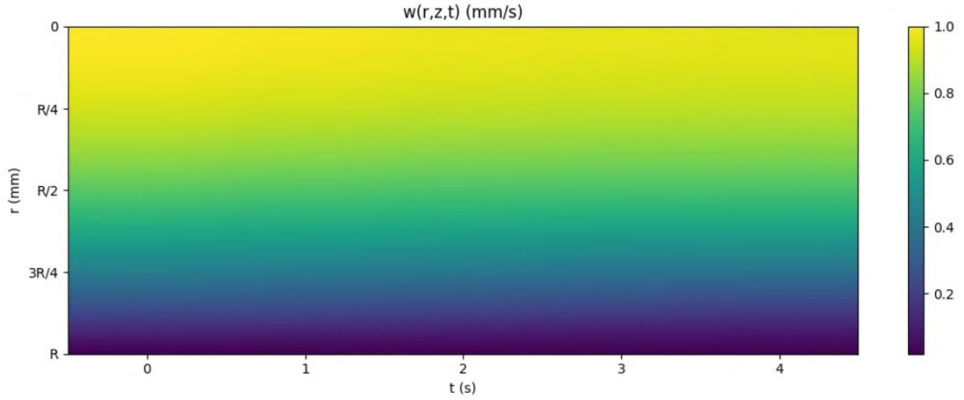

Figure 4: PINN output for a steady Poiseuille pipe flow with 100 simulated tracer particles distributed throughout a 2 mm long pipe segment for 4s.

4.3.1 Impact of seeding density

The number of simulated tracer particles (i.e, experimental data points) greatly impacts the training and accuracy of our PINN. In order to study the constraints on our data quantity necessary for our PINN to work to the desired accuracy, we test the PINN with varying the quantity of our data. Figure 6 shows the L2 norm of the error on the w component of the velocity vector at 0s as the seeding density is increased. The error is plotted on a log scale. As expected, the error decreases with increasing the experimental data for a fixed training time of 1 hour.

4.3.2 Impact of activation function

The impact of choice of the hidden layers activation function on the accuracy of the PINN is studied by testing with a hyperbolic tangent. The L2 norm of the error on the w component of the velocity increases by an order of magnitude for the seeding of 100 particles from 25.47 to 34.34 with the hyperbolic tangent which shows that the sigmoid is a better activation function to introduce the nonlinearity in our case.

4.3.3 Impact of training time

Lastly, we also look at the impact of the training and increase the training time from 1 hour to 2 hours. The L2 norm of the error on the w component of the velocity vector using the hyperbolic tangent activation function decreases from 34.34 to 19.86. This indicates, as expected, that the longer we train for, the more accurate the PINN output will be.

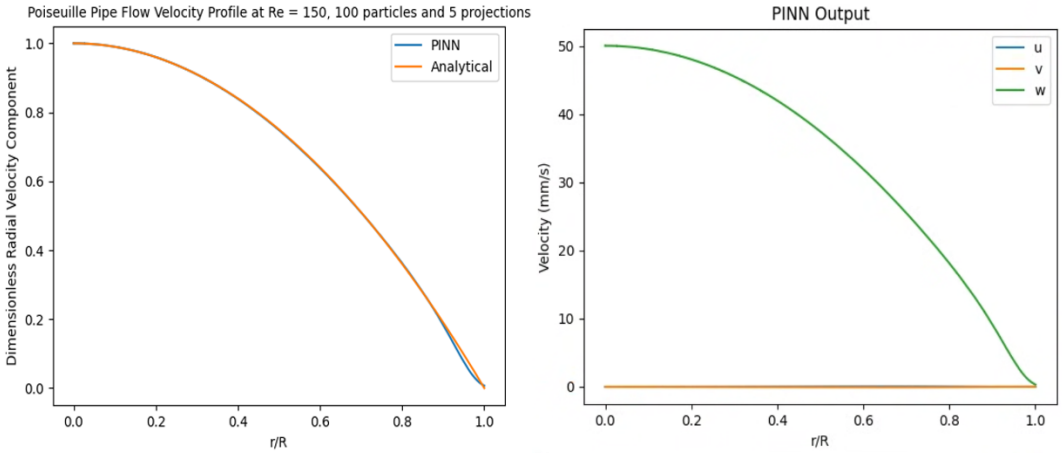

Figure 5: PINN output at one time instant for a steady Poiseuille pipe flow with 100 simulated tracer particles distributed throughout a 2 mm long pipe segment.

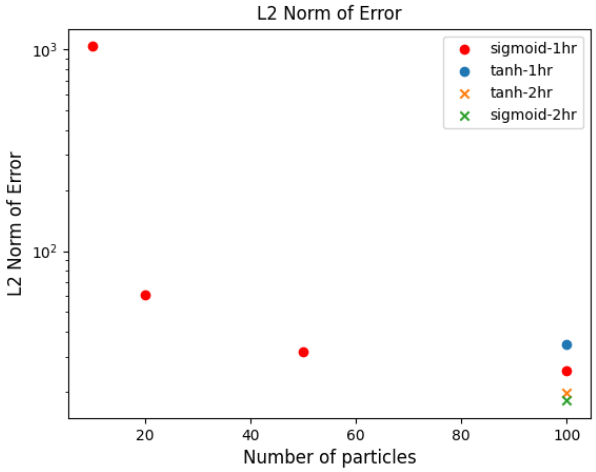

Figure 6: L2 norm of the error on the w component of the velocity for different activation functions and as the number of particles increases

5. Discussion

We find that the use of PINNs has great potential to advance XPV and expand the realm of flows that can be studied. Its true strength lies in generating a full flow picture from a few sparse measurements through leveraging the knowledge of physics, i.e. Navier Stokes equations and boundary conditions. We have proven that with a few measurements we can infer the full flow velocity profile for a Poiseuille flow while ensuring the solution complies with physics.

In future work, the effect of tracer position uncertainty and data sparsity will be investigated in more depth by simulation and experimentation. We will expand to flows where density and phase change occur [6,7] in order to be able to compare to [12]. The cost function will be engineered further to account for uncertainty in particle trajectories due to noise, particle overlaps as well as incorporate an adaptive weighting scheme for regions in the flow that have data and regions that are being resolved solely based on physics.

In a follow-on paper being prepared, we elaborate on how we go from from a single source-detector pair to the full flow visualization using PINNs. We initially obtain limited SNR data from one angle at one instant in time, as indicated in Figure 2 then identify the particles utilising rCNN, then resolve the

trajectories using a limited angle tracking code. The data is, finally, used to train the PINN as described in this paper.

6. Conclusions

In this work, we have presented on the use of PINNs to advance XPV as an experimental method for visualizing flows. We have taken the case of a simple Poiseuille flow that is well understood and has an analytical solution to train our PINN. Training was done using the Navier Stokes momentum and mass continuity equations and sparse XPV data on an NVIDIA RTX A4500 GPU for approximately 9000 epochs for a training time of 1 hour for the single time instant data and 4 hours for the results shown in Figure 4. The impact of factors such as the training time, the activation function and the number of particles on the accuracy of the PINN was also studied. As with all neural networks, the error decreases as the number of data points and the training time is increased.

7. Acknowledgements

This work was partly supported by AFRI Competitive Grant no. 2020–67021-32855/project accession no. 1,024,262 from the USDA National Institute of Food and Agriculture. This grant is being administered through AIFS: the AI Institute for Next Generation Food Systems. https://aifs.ucdavis.edu.

8. References

[1] Mäkiharju, S. A., Dewanckele, J., Boone, M., Wagner, C., & Griesser, A. (2022). Tomographic X-ray particle tracking velocimetry: Proof-of-concept in a creeping flow. Experiments in Fluids, 63, 1-12.

[2] Parker, J. T., & Mäkiharju, S. A. (2022). Experimentally validated x-ray image simulations of 50 μm x-ray PIV tracer particles. Measurement Science and Technology, 33(5), 055301.

[3] Parker, J. T., DeBerardinis, J., & Mäkiharju, S. A. (2022). Enhanced laboratory x-ray particle tracking velocimetry with newly developed tungsten-coated O (50 μm) tracers. Experiments in fluids, 63(12), 184.

[4] Parker, J. T., Dreier, T., Nilsson, D., & Mäkiharju, S. A. (2024). In-lab X-ray particle velocimetry for multiphase flows: Design principles and demonstration of O (1 kHz) XPV. Flow Measurement and Instrumentation, 96, 102536.

[5] Parker, J. T., Consiglio, A. N., Rubinsky, B., & Mäkiharju, S. A. (2024). Direct comparison of isobaric and isochoric vitrification of two aqueous solutions with photon counting X-ray computed tomography. *Cryobiology*, *114*, 104839.

[6] Ali, A. M., Chang, B., Consiglio, A. N., Van Moer, G. S., Powell-Palm, M. J., Rubinsky, B., & Mäkiharju, S. A. (2024). Experimental observation of cavity-free ice-free isochoric vitrification via combined pressure measurements and photon counting x-ray computed tomography. Cryobiology, 116, 104935.

[7] Raissi, M., Yazdani, A., & Karniadakis, G. E. (2020). Hidden fluid mechanics: Learning velocity and pressure fields from flow visualizations. Science, 367(6481), 1026-1030.

[8] Wang, H., Liu, Y. and Wang, S., 2022. Dense velocity reconstruction from particle image velocimetry/particle tracking velocimetry using a physics-informed neural network. Physics of fluids, 34(1).

[9] Hasanuzzaman, G., Eivazi, H., Merbold, S., Egbers, C., & Vinuesa, R. (2023). Enhancement of PIV measurements via physics-informed neural networks. Measurement Science & Technology, *34*(4), 44002-. https://doi.org/10.1088/1361-6501/aca9eb

[10] Mao, Z., Jagtap, A. D., & Karniadakis, G. E. (2020). Physics-informed neural networks for high-speed flows. Computer Methods in Applied Mechanics and Engineering, *360*, 112789-.

[11] Yin, M., Zheng, X., Humphrey, J. D., & Karniadakis, G. E. (2021). Non-invasive inference of thrombus material properties with physics-informed neural networks. Computer Methods in Applied Mechanics and Engineering, *375*, 113603-.

[12] Rabin, Y. (2021). Mathematical modeling of surface deformation during vitrification. Cryobiology, 102, 34-41.